Spectral methods for analyzing energy balances in geodynamo simulations

Margaret S. Avery[a,c,*], Catherine G. Constable[a], Christopher J. Davies[b], David Gubbins[b,a]

[a]*Scripps Institution of Oceanography, University of California, San Diego, La Jolla, CA 92093, U.S.A.*

[b]*School of Earth and Environment, University of Leeds, Leeds, LS29JT, U.K.*

[c]*Earth and Planetary Science, University of California, Berkeley, Berkeley, CA 94720, U.S.A*

Abstract

Spectral methods can be applied to evaluate the detailed products available from geodynamo simulations but inaccessible in the paleomagnetic record. These spectral methods are well developed but have not previously been applied to studying the energy balance of geodynamo simulations. We illustrate these ideas by analyzing output from numerical dynamo simulations which have previously been studied for their apparently Earth-like properties. Consistently high coherence levels are observed between the total magnetic energy in the outer core and the paleomagnetically observable energy in the axial dipole moment at frequencies below 0.01 kyr^{-1}. Between 0.01 and 0.1 kyr^{-1} there is a fall off in coherence; at higher frequency the coherence is negligible. Assessments of coherence specta between rates of change in kinetic and magnetic energy, ohmic and viscous dissipations, and work done by the buoyancy and Lorentz forces facilitate testing hypotheses about changes in the energy

*Corresponding author

Email address: `msavery@berkeley.edu` (Margaret S. Avery)

balance in geodynamo simulations as a function of frequency. An important characteristic of the recent geomagnetic field is that on average the axial dipole has been observed to grow more rapidly than it decays. This behavior is frequency dependent and observed when signal of frequencies higher than 0.03 kyr^{-1} have been filtered out. This provides a useful criterion for evaluating geodynamo simulations using spectral methods, because the frequency dependence of poloidal axial dipole energy at Earth's surface reflects the balance of diffusive and advective processes in Earth's core.
Keywords: geomagnetic dipole variations, numerical geodynamo simulations, outer core energy balance, spectral analysis

1. Introduction

The geomagnetic field is an important component of our planetary environment that varies over a broad range of frequencies (Constable and Johnson, 2005). Paleomagnetic observations record the behavior of the geomagnetic field in the past and tell us about the inner workings of the planet; however, the record is noisy and incomplete. A fruitful approach for investigating long-term paleo-secular variation that overcomes these limitations is to compare observations of Earth's magnetic field with the statistical properties of magnetic fields generated by numerical geodynamo simulations. Dynamo simulations do not suffer from observational noise or sparseness and their internal dynamics can be subjected to detailed study. Our goal in this work is to gain deeper understanding of variations in the axial dipole strength observed in the paleomagnetic record by analyzing the conversion of kinetic energy to magnetic energy and dissipation of these energies as functions of frequency in geodynamo simulations.

There is a trade off in paleosecular variation observations between timespan and spatial resolution – further back in time we have less information about the field's temporal variations. For the modern field we have high resolution observations from satellites and geomagnetic observatories, but they span a small portion of the geomagnetic field's spectrum of variations. These high resolution geomagnetic observations can be inverted for core flow at the core mantle boundary (CMB) by making a 'frozen-flux' approximation that the fluid has infinite electric conductivity and additional assumptions to overcome the non-uniqueness of the problem (Bloxham and Jackson, 1991). The resulting flows can then be linked to core dynamics found in geodynamo simulations; there is evidence for features such as a high-latitude polar jet in the northern hemisphere (Livermore et al., 2017) and a planetary-scale gyre in the southern hemisphere (Finlay et al., 2016). In the Holocene field reconstructions there is evidence of high-latitude flux patches in both northern and southern hemispheres that vary in strength and position (e.g. Bloxham and Gubbins, 1985; Johnson and Constable, 1998; Korte and Holme, 2010) and evidence of spatial heterogeneity in field activity, with more activity in the southern hemisphere (Constable et al., 2016). These features cannot be link directly to core flow. The paleomagnetic dataset from the past 10 kyr (Holocene) has enough spatial and temporal resolution to build low degree spherical harmonic representations of the field variations but not enough to invert for core flow (e.g. Constable et al., 2016).

On timescales longer than 10 kyr, which is the focus of this work, there are not yet models of paleomagnetic field variations with higher spatial resolution than the axial dipole moment (ADM). SINT2000 and PADM2M are two examples of ADM models spanning the past 2 Ma (Valet et al., 2005; Ziegler et al., 2011). These ADM models have power spectral densities that decrease with frequency – above a corner frequency of $\sim 10^{-2}$ kyr^{-1} their spectral fall off at a rate of $f^{-7/3}$ (Ziegler and Constable, 2011). On the longest timescales (10^8 yrs) only the paleomagnetic polarity timescale is well defined (Cande and Kent, 1992, 1995). It is unclear how to relate these variations to core dynamics. To compare with paleomagnetic ADM variations we are interested in dynamo variations with frequencies between 10^{-2} and 10^{-1} kyr^{-1}.

Here we use spectral analysis methods to assess the frequency dependence of geodynamo processes indicated by the broad spectrum of geomagnetic activity. We use spectral methods to link the observable surface ADM with with core variations, and then to 'look inside' the core at the balance of energies. Previous studies of geodynamo simulations have assessed the conversion of kinetic energy to magnetic energy and dissipation of these energies (e.g. Olson et al., 1999; Buffett and Bloxham, 2002; Nimmo, 2015), but not as a function of frequency as we do.

An example of a frequency dependent phenomenon observed in the paleomagnetic record is an asymmetric growth and decay of the ADM (Ziegler and Constable, 2011; Avery et al., 2017). This is seen when high frequency variations are removed from paleomagnetic ADM models. In the underlying, lower-frequency signal the axial dipole moment grows more rapidly than it decays. This behavior is found in different magnetic recording materials: Ziegler and Constable (2011) identified asymmetry in the PADM2M field model which has ADM variations constrained by calibrated sedimentary records, and Avery et al. (2017) observed it in the thermal remanent magnetization recorded in the seafloor. The asymmetric behavior is not just associated with polarity reversals; it appears to be an important characteristic of secular variation. Studying this behavior could help understand the context of present day geomagnetic field variations, dynamics of the unobservable portions of the field, and the role of diffusion in ADM variations. A plausible interpretation of the asymmetry is that decreasing dipole moment is dominated by slow diffusive processes, while on the same timescales dipole field growth occurs more rapidly and is controlled by the induction of field by fluid advection (Ziegler and Constable, 2011). Here we demonstrate the utility of spectral methods to understand the link between CMB and whole-core processes, and to evaluate the mechanism for asymmetry between axial dipole growth and decay rates in geodynamo simulations as functions of frequency.

We begin by describing the geodynamo simulations we use and define the components of their energy balance (Section 2.1). We then describe our method of evaluating the asymmetry in ADM rates of change (Section 2.2) and our time series analysis of the outer core energy balance (Section 2.3). Using standard tools of spectral analysis, we evaluate the link between the total magnetic energy present in the outer core and the dipole energy observed at Earth's surface and assess the energetics. We then describe the paleomagnetic ADM reconstruction PADM2M (Sections 2.4). We choose two illustrative geodynamo simulations from Davies and Gubbins (2011) because they have long timespans and were determined to be Earth-like by other criteria, thus warranting further study (Davies and Constable, 2014). Results are presented in Section 3 and discussed in Section 4, and finally our conclusions are summarized in Section 5.

2. Methods

2.1. Geodynamo simulations

The dynamo solutions we use here have been previously described, and a detailed explination of the code and solution technique can be found in Willis et al. (2007) and Davies and Gubbins (2011). A rotating spherical shell of thickness $d = r_o - r_i$ (where r_o is the outer radius, r_i the inner, and $r_i/r_o = 0.35$) is filled with incompressible, electrically conducting Boussinesq fluid. It rotates at a rate Ω, and has constant thermal diffusivity κ, magnetic diffusivity η, coefficient of thermal expansion α, and viscosity ν. The nondimensional numbers are the Ekman number, the Prandtl number, the magnetic Prandtl number and the Rayleigh number:

$$E = \frac{\nu}{2\Omega d^2}, \qquad Pr = \frac{\nu}{\kappa}, \qquad Pm = \frac{\nu}{\eta}, \qquad Ra = \frac{\alpha g \beta d^5}{\nu\kappa} \tag{1}$$

where g is the acceleration due to gravity and β is the temperature gradient at the outer boundary. The Ekman number describes the ratio between viscous and Coriolis forces. The Rayleigh number indicates the presence and vigor of convection (if $Ra > Ra_{cr}$ where Ra_{cr} is the critical Ra for the onset of convection).

Analysis of variations in magnetic and kinetic energy of the geodynamo models provides a means of examining their internal dynamics. The induction equation governs changes magnetic field caused by induction and dissipation, and the momentum equation governs changes in fluid velocity generated by buoyancy and lost by work done on the magnetic field and viscous dissipation.

Global balances of magnetic and kinetic energy are found by respectively taking the dot product of the induction equation with $\mathbf{B}/\mu$, the dot product of the momentum equation with $\mathbf{u}$, then integrating over the volume of the core:

$$\dot{M} = -L - O \tag{2}$$

and

$$\dot{K} = G + L - V, \tag{3}$$

where $\dot{x}$ notation indicates the time derivative of x. M and K are the magnetic and kinetic energy densities defined as:

$$M = \frac{Pm}{2E} \int \mathbf{B}^2 dV_s \tag{4}$$

and

$$K = \frac{1}{2} \int \mathbf{u}^2 dV_s, \tag{5}$$

where $\mathbf{B}$ is the magnetic field, $\mathbf{u}$ is the fluid velocity.

$$O = \frac{Pm}{E} \int (\nabla \times \mathbf{B})^2 \, dV_s, \tag{6}$$

$$L = \frac{Pm}{E} \int \mathbf{u} \cdot (\mathbf{j} \times \mathbf{B}) \, dV_s, \tag{7}$$

$$V = Pm \int (\nabla \times \mathbf{u})^2 \, dV_s, \text{and} \tag{8}$$

$$G = \frac{(Pm)^2 \; Ra}{Pr} \int (u_r \vartheta) \, dV_s \tag{9}$$

are the ohmic dissipation, the work done by the Lorentz force, the viscous dissipation, and the work done by the Buoyancy force. $\mathbf{j}$ is current density, u_r radial velocity, and ϑ temperature fluctuation.

The energy and dissipation terms M, K, O, and V are outputs of our simulations and plotted in Figure S2 of the supplementary materials. Generally, the magnetic energy and ohmic dissipation vary in phase, the kinetic energy and viscous dissipation vary in phase, and the kinetic and magnetic energy are out of phase. We compute $\dot{M}$ and $\dot{K}$ analytically after fitting a cubic B-spline function to time series of M and K. The changes in the kinetic energy ($\dot{K}$) and viscous dissipation (V) are much more important in these simulations than we expect for the Earth. The work done by the Lorentz force, L, and the work done by the Buoyancy force, G, are then obtained from Equations 2 and 3.

Table 2 provides a summary of the numerical parameters and physical characteristics for the two simulations. We compare the time averages (denoted by $\langle\rangle$) and standard deviation (σ) of the dimensionless axial dipole spherical harmonic Gauss coefficient (g_1^0), the length scales for magnetic and viscous dissipation as defined in Oruba and Dormy (2014)

$$\ell_B^2 \equiv \frac{\int_{V_s} \mathbf{B}^2 \mathrm{d}V_s}{\int_{V_s} (\nabla \times \mathbf{B})^2 \mathrm{d}V_s}, \qquad \ell_u^2 \equiv \frac{\int_{V_s} \mathbf{u}^2 \mathrm{d}V}{\int_{V_s} (\nabla \times \mathbf{u})^2 \mathrm{d}V_s}, \tag{10}$$

and the amplitude of the magnetic ($Lo = \sqrt{2M/V_s}$) and velocity fields ($Rm = \sqrt{2K/V_s}$).

Table 1: Definitions of variables used throughout the text.

Input			
d	shell of thickness	V_s	non-dimensional volume of the outer core
r_o	outer core radius	r_i	inner core radius, and $r_i/r_o = 0.35$
t	time	f	frequency
g	acceleration due to gravity	Ω	rotation rate
β	temperature gradient at the outer boundary	α	coefficient of thermal expansion
κ	thermal diffusivity	η	magnetic diffusivity
ν	viscosity	ϑ	temperature fluctuation
$\mathbf{j}$	current density	$\mathbf{B}$	magnetic field
$\mathbf{u}$	velocity field	u_r	radial velocity
E	Ekman number, $\frac{\nu}{2\Omega d^2}$	Ra	Rayleigh number, $\frac{\alpha g \beta d^5}{\nu\kappa}$
Pr	Prandtl number, $\frac{\nu}{\kappa}$	Pm	magnetic Prandtl number, $\frac{\nu}{\eta}$
Output			
M	magnetic energy integrated over the outer core	Lo	amplitude of the magnetic field, $\sqrt{2M/V_s}$
K	total kinetic energy integrated over the outer core	Rm	amplitude of the velocity field, $\sqrt{2K/V_s}$
ℓ_B	length scale of the magnetic dissipation	ℓ_u	length scale of the viscous dissipation
O	ohmic dissipation	L	work done by the Lorentz force
V	viscous dissipation	G	work done by the buoyancy force
Analysis			
$g_1^0(t)$	axial dipole spherical harmonic Gauss coefficient	$R_1^0(t)$	non-dimensional surface axial dipole energy
s	normalized skewness coefficient	f_{co}	cutoff frequency, corner f of low-pass filter
ς_s	bootstrap estimate of s standard error	$A_{X,X}(t)$	autocovariance for time series $X(t)$
$\widetilde{X}(f)$	power density spectrum for time series $X(t)$	$\widetilde{X,Y}(f)$	cross spectrum between two time series
$\overbrace{XY}(f)$	coherence spectrum between two time series	Δf	frequency resolution of spectral estimate

Table 2: Comparison of numerical parameters and time-averaged physical properties of our two test geodynamo simulations. $\langle\rangle$ indicates time averaging and σ is the standard deviation. Numbers in parentheses are normalized to values for Case 2.2. Variables are defined in Table 1. Non-dimensionalized PADM2M has $\langle g_1^0 \rangle = 1.712 \times 10^{-2}$, $\sigma_{g_1^0} = 0.48 \times 10^{-2}$.

Parameter	**Case 2.2**	**Case 2.3**
RaE	20	50
Cooling rate	moderate 69 K/Gyr	moderate 69 K/Gyr
$\langle Rm \rangle$	78	105
$\langle Lo \rangle$	114	164
$\langle g_1^0 \rangle$	1.52×10^{-2}	2.65×10^{-2}
$\sigma_{g_1^0}$	0.15×10^{-2}	0.25×10^{-2}
$\langle \ell_B \rangle$	9.50×10^{-2}	8.02×10^{-2}
$\langle \ell_u \rangle$	7.01×10^{-2}	6.32×10^{-2}

2.2. ADM energy evaluation

To compare dipole moment variations observed in PADM2M with the products of numerical geodynamo simulations (which are energies and therefore quadratic quantities) we non-dimensionalize PADM2M's g_1^0 coefficients with $\sqrt{2\Omega\rho\mu\eta}$ (Davies and Constable, 2014), and then we compute the non-dimensional surface axial dipole energy,

$$R_1^0(t_i) = 2\left|g_1^0(t_i)\right|^2, i = 1, 2, ...n. \tag{11}$$

This is the axial dipole ($l = 1$, $m = 0$) term of the Mauersberger-Lowes geomagnetic spectrum (Lowes, 1974) at each time t_i, $i = 1, 2, ...n$, where n is the number of time samples. Its time derivatives are given by

$$\dot{R}_1^0(t_i) = 4\left|g_1^0(t_i)\right|\left|\dot{g}_1^0\right|(t_i). \tag{12}$$

The geomagnetic R_1^0 and $\dot{R}_1^0$ from PADM2M are plotted in Figure 1a–b, and R_1^0 for our dynamo simulations are plotted in supplementary figure S2a–b. Here, as with the axial dipole moment Gauss coefficient g_1^0, the sub- and superscripts indicate the degree and order ($l = 1$, $m = 0$) of the geomagnetic energy term.

To compare the temporal variations of dynamo simulations with these observations we rescale simulation time using the magnetic diffusion timescale d^2/η = 232,000 years ($\eta = 0.7$ m^{2}s^{-1}, Pozzo et al., 2012, 2013). Davies and Constable (2014) argued that this time scaling is an appropriate choice for these simulations when comparing them to long timescale behavior of PADM2M. Olson et al. (2012) also studied power spectra of axial dipole momens, and they used advective scaling to better align the spectra of simulations with different Rm values at high frequencies (Rm = 170–1985). We compare the power spectra of g_1^0 with diffusive and advective frequency scaling in supplementary Figure S3. We choose to use diffusive scaling because it better matches the intermediate and low frequency (< 0.1 kyr^{-1}) ADM variations of PADM2M we are studying here. Davies and Constable (2014) showed that our selected dynamo simulations have been run past the point where their g_1^0 has a stable time average (i.e. the time period past which produces in the time averaged g_1^0 of $< 1\%$). We therefor frequently reference the longest time averages available in the simulations since these are close to steady state. Steady state is a convenient reference point for understanding the energy balance in these dynamo simulations.

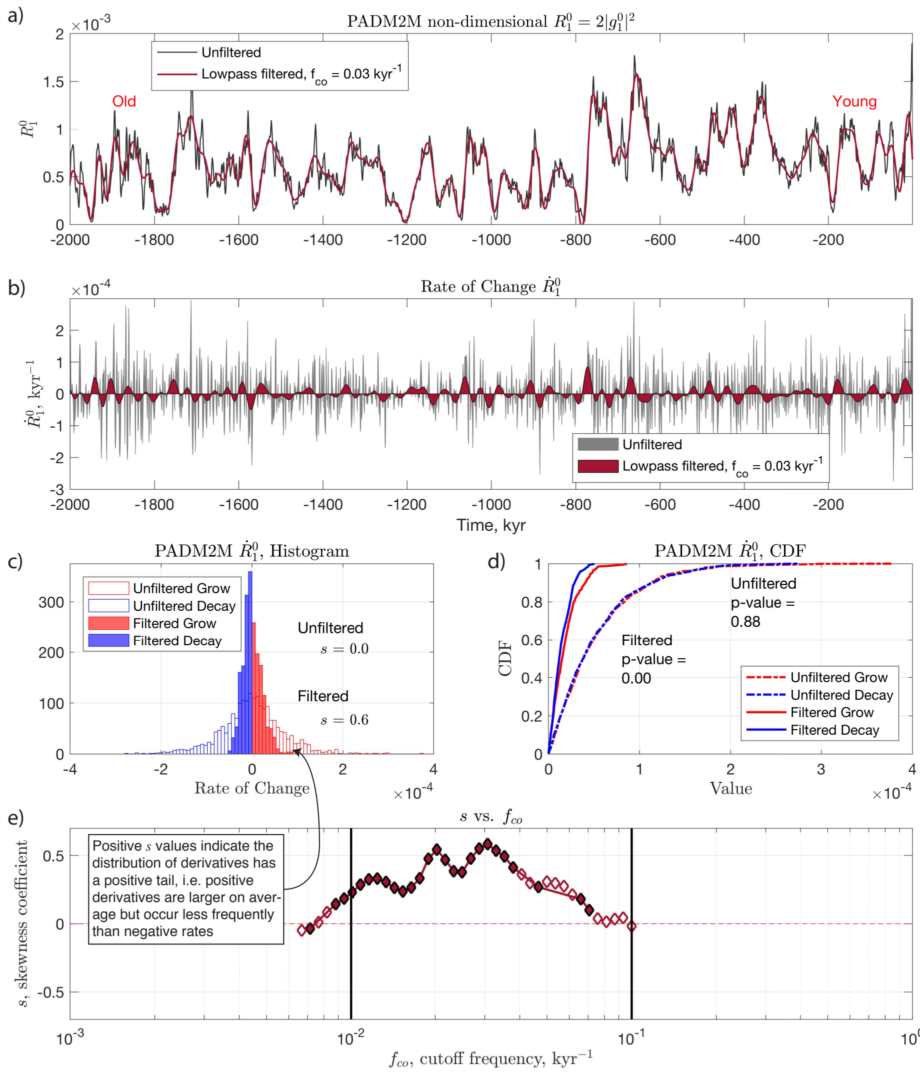

Figure 1: A summary of the distribution of axial dipole energy derivatives after low-pass filtering with various corner frequencies. a) The time series of non-dimensional surface dipole energy R_1^0 for the paleomagnetic field model PADM2M. b) The time series of time derivatives of R_1^0. In panels a and b the grey lines are unfiltered, and the red lines have been low-pass filtered with a cutoff frequency of 0.03 kyr^{-1}. c) The distribution of PADM2M $\dot{R}_1^0$ before filtering (open bars), and after filtering with a low-pass corner frequency of 0.03 kyr^{-1}. After filtering the distribution has a positive tail. d) The cumulative distribution functions, CDFs, of PADM2M positive (red) and negative (blue) $\dot{R}_1^0$ before filtering (dashed lines), and after filtering with a low-pass corner frequency of 0.03 kyr^{-1} (solid lines). e) The skewness is parameterized as the $s(f_{co})$ of $\dot{R}_1^0$. See text and Equation 13 for details. Open symbols indicate a p-value > 0.05 in the two-sample Kolmogorov-Smirnov test as discussed in the text.

Following the method described by Avery et al. (2017) for parameterizing the distribution of ADM derivatives, we exclude variations below the specified cutoff frequency f_{co}, by applying a Parks-McClellan equiripple low-pass filter (Parks and McClellan, 1972) to the time series of time derivatives. The power spectrum of the time derivatives of PADM2M before and after applying a low-pass filter is plotted in supplementary Figure S4. Avery et al. (2017) found a robust estimate of asymmetry is provided by the geomagnetic skewness coefficient for the distribution of dipole field derivatives. Here we apply this method to the energy term $\dot{R}_1^0(t_i)$ to make comparison between our results and the other products of the geodynamo simulations easier. The skewness of a distribution of the axial dipole energy derivatives is the third moment about the mean, which is rendered dimensionless by normalizing by the standard deviation cubed. The result is the skewness coefficient, s

$$s = \frac{\frac{1}{n}\sum_{i=1}^{n}\left(\dot{R}_1^0(t_i) - \langle\dot{R}_1^0\rangle\right)^3}{\left(\sqrt{\frac{1}{n}\sum_{i=1}^{n}\left(\dot{R}_1^0(t_i) - \langle\dot{R}_1^0\rangle\right)^2}\right)^3}. \tag{13}$$

ς_s is the standard error of s and was estimated by bootstrap resampling of independent and identically distributed blocks of $\dot{R}_1^0$. This is described in detail in the supplementary materials.

A two-sample Kolmogorov-Smirnov test between the cumulative distribution functions of the positive and negative derivatives was used to test for departures from the null hypothesis that they are from populations with the same distribution at the 95% significance level. Distinguishable distributions are indicated with closed symbols in Figures 1 and 2. The p-value is the probability of acquiring as large a KS statistic when the two sample distributions come from the same empirical distribution, if $p > 0.05$ this null hypothesis is rejected at the 95% significance level.

2.3. Frequency domain spectral analysis

Consider two time series labeled $X(t)$ and $Y(t)$. The power spectrum ($\widetilde{X}(f)$) of the time series X is defined as

$$\widetilde{X}(f) = \mathfrak{F}\left[A_{X,X}(t_1,t_2)\right] = \int_{-\infty}^{\infty} \mathcal{E}\left[(X(t_1) - \langle X\rangle)(X(t_2) - \langle X\rangle)\right] e^{-2\pi i f t} dt, \tag{14}$$

where $\mathfrak{F}$ denotes the Fourier transform, $A_{X,X}(t_1,t_2) = \mathcal{E}\left[(X(t_1) - \langle X\rangle)(X(t_2) - \langle X\rangle)\right]$ is the autocovariance, and $\mathcal{E}[x]$ indicates the expectation value of x. $\widetilde{X}(f)$ describes how much variance the time series $X(t)$ has as a function of frequency.

The coherence spectrum $\overbrace{XY}(f)$ between the two time series is the squared magnitude of the cross-spectrum i.e. the Fourier transform of the cross-covariance of the two series normalized by the power spectra of the two series,

$$\overbrace{XY}(f) = \frac{\left|\widetilde{X,Y}(f)\right|^2}{\widetilde{X}(f)\widetilde{Y}(f)} \tag{15}$$

where the cross spectrum is defined as

$$\widetilde{X,Y}(f) = \mathfrak{F}\left[\mathcal{E}\left[X(t)Y(t+dt)\right]\right] = \int_{-\infty}^{\infty} \mathcal{E}\left[X(t)Y(t+dt)\right] e^{-2\pi i f t} dt. \tag{16}$$

$\overbrace{XY}(f)$ gives a correlation coefficient between the two signals as a function of frequency. A value of one would indicate that the two time series are perfectly correlated at that frequency. To estimate these spectra we used a sine multitaper method based on the theory of Riedel and Sidorenko (1995).

We prewhitened the spectra, as is recommended for red spectra. Typical frequency resolution, Δf, of the spectra for the cases are shown in Figure 3 c–d.

First we evaluate the ability of the ADM to carry information about the outer core energy as a function of frequency using both the coherence spectra between the total magnetic energy integrated over the outer core and the surface axial dipole energy $(\overbrace{MR_1^0}(f))$ and the coherence between the total $l = 1$ magnetic energy dipole energy integrated over the outer core and the surface axial dipole energy $(\overbrace{M_1^{0,1}R_1^0}(f))$. The sub and superscripts of $M_1^{0,1}$ - as with g_1^0 and R_1^0 - indicate the $l = 1$ and $m = 0, 1$ term of the magnetic energy integrated over the outer core, M.

Using the power spectral density and the coherence spectra we assess changes in the energy balance as a function of frequency. We track the conversion of kinetic to magnetic energy as a function of frequency over a broad range. We estimate the PSDs $\widetilde{\dot{M}}(f)$, $\widetilde{O}(f)$, $\widetilde{L}(f)$, and the squared coherence spectra $\overbrace{\dot{M}O}(f)$, $\overbrace{\dot{M}L}(f)$, and $\overbrace{OL}(f)$ to evaluate the balance of terms in Equation 2. We estimate the PSDs of $\widetilde{\dot{K}}(f)$, $\widetilde{V}(f)$, $\widetilde{G}(f)$ and $\widetilde{L}(f)$, and the squared coherence spectra $\overbrace{VL}(f)$, $\overbrace{VG}(f)$, and $\overbrace{\dot{K}L}(f)$ to evaluate the balance of terms in Equation 3. Then to test if low frequency changes in the ohmic and viscous dissipations are associated with changes in the length scale or amplitude of the magnetic field and velocity field respectively we evaluate the squared coherence spectra $\overbrace{O\ell_B}(f)$, $\overbrace{OLo}(f)$, and $\overbrace{V\ell_u}(f)$, $\overbrace{VRm}(f)$, where ℓ_B and ℓ_u are the length scales of the magnetic field and velocity, and Lo and Rm are the non-dimensional amplitudes of the magnetic field and velocity.

2.4. Paleomagnetic ADM model

We use the representation of the paleomagnetic field provided by the 2 Myr model of axial dipole moment PADM2M. Ziegler et al. (2011) constructed PADM2M using a penalized maximum likelihood inversion technique and 76 sedimentary relative paleointensity records calibrated by absolute paleointensity data to produce a continuous, time-varying model of ADM; temporal variations were modeled with a cubic B-spline, allowing time derivatives to be calculated analytically. PADM2M resolves ADM variations on timescales of about 10 kyr and longer. The PADM2M model as well as its first and second time derivatives evaluated every 1 kyr are available through the EarthRef.org Digital Archive (ERDA, earthref.org/ERDA/1138/).

3. Results

The results of our analyses of the dynamo simulations are presented in Figures 2–6, and for the purpose of discussion we consider three frequency ranges: low (< 0.01 kyr^{-1}), intermediate ($0.01 - 0.1$ kyr^{-1}), and high (> 0.1 kyr^{-1}) indicated by the black vertical lines. These ranges were chosen to loosely match the ranges where ADM skewness is absent or present for PADM2M (Figure 1), though we do not expect the variations of the simulations to perfectly match these frequency ranges because rescaling the time is likely to be imperfect.

3.1. PADM2M

In the unfiltered PADM2M series the time spent growing and decaying is balanced, but the low-pass filtering uncovers an imbalance in the rates of change: positive derivative values, which correspond to a growing dipole, are larger on average and occur less frequently than negative rates representing decay i.e. the distribution has a positive tail (Figure 1). After low-pass filtering this two sample KS test shows the positive and negative CDFs come from different distributions (Figures 1d).

At low frequencies PADM2M shows no skewness in its $s(f_{co})$ and the $\dot{R}_1^0$ derivatives are small in amplitude, from this we hypothesize at low frequencies the geodynamo is in quasi-steady state and the $\dot{M}$ term is small compared to the O and L terms. At intermediate frequencies where PADM2M displays a skewed distribution of $\dot{R}_1^0$ this steady state breaks down. Slower average decay of the dipole suggests periods where the field is dominated by large scale diffusion, and the faster average growth suggest advection is acting to increase the dipole strength. At higher frequencies PADM2M has little resolution and the record is likely dominated by small, random advective fluctuations.

3.2. Geodynamo Simulations

Geodynamo simulations are able to produce first order features of the geomagnetic field such as a dominantly dipolar structure and polarity reversals. However, because of computational restrictions none of these simulations are realistic models of the Earth's geodynamo; they cannot be run with sufficiently rapid rotation, thermal diffusivity, and low viscosity characteristic of the Earth's outer core. Previous studies have defined criteria for determining the degree of similarity between the fields produced by geodynamo simulations and the geomagnetic field. Christensen et al. (2010) compared simulations to the geomagnetic field based on field morphology at the core-

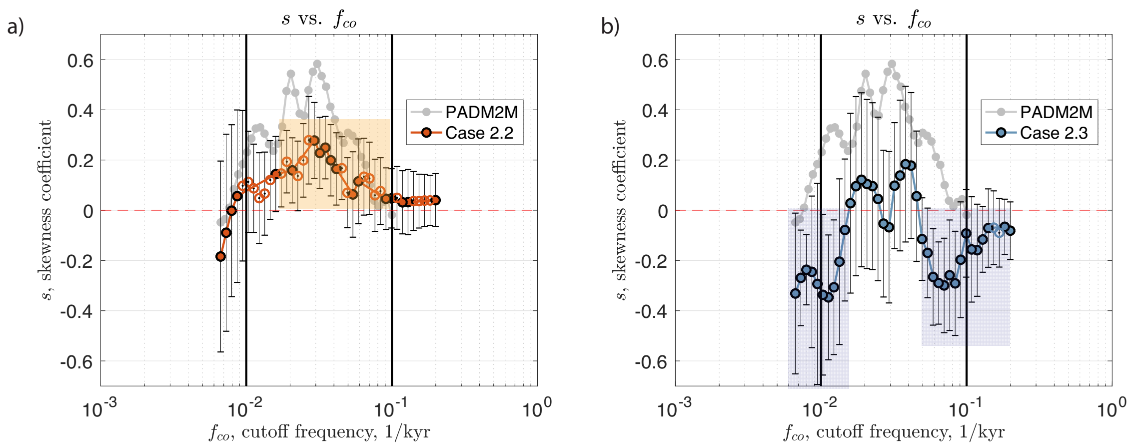

Figure 2: Axial dipole energy skewness results for geodynamo simulations cases. $s(f_{co})$ for a) Case 2.2 (orange), and b) Case 2.3 (blue), grey dots show PADM2M result. Case 2.2 has $s(f_{co})$ that shows a similar pattern to that seen in the Earth (Figure 1e). Error bars are $\pm 1\ \varsigma_s$(the standard error of s estimated using a bootstrap method). Open symbols indicate a p-value > 0.05 in the two-sample Kolmogorov-Smirnov test as discussed in the text. The orange rectangle in highlight where Cases 2.2 has positive $s(f_{co})$. The blue checkered rectangles highlight were Cases 2.3 has negative $s(f_{co})$.

mantle boundary (computing the relative strength of the dipole, equatorial symmetry, zonality, and presence of flux concentration), finding Earth-like field morphologies for a limited range of simulation input parameters. Davies and Constable (2014) introduced a criterion to identify dynamos with Earth-like long-term temporal behavior by determining whether the power spectrum of the ADM could be fit with the same frequency dependent power law as observed in the PADM2M empirical model. Mound et al. (2015) added a criterion that compares the secular variation of their simulated radial magnetic field at the CMB to the observed quiet Pacific, where secular variation is weak.

Our study dynamo simulations were drawn from Davies and Gubbins (2011) (their cases 2.2 and 2.3), and were selected because of their long run times (10 and 3 magnetic diffusion times respectively) and their Earth like field morphologies. They both have $E = 1.2 \times 10^{-4}$, $Pm = 2$, $Pr = 1$, a mix of bottom and internal heating, homogeneous outer boundary heat flux, and fixed temperature inner boundary. Cases 2.2 and 2.3 have buoyancy profiles that model a moderate cooling rate resulting in an inner core age of 614 Myr (Gubbins et al., 2004). The difference between the cases is Ra: Case 2.2 has $Ra = 20$ and Case 2.3 has $Ra = 50$. Both cases are dipole dominated, do not reverse over the duration of the run, and were found to be Earth-like when the dimensionless simultions time is rescaled by the magnetic diffusion time (Davies and Constable, 2014). Cases 2.2 and 2.3 are compatible morphologically with the paleomagnetic field model CALS3k.4b, and their ADM power spectra have similar structure to PADM2M's (Davies and Constable, 2014).

More vigorous convection in Case 2.3 leads to smaller length scales of the velocity and magnetic field. With increased Ra Case 2.3 has higher - and more variable - magnetic field strength and velocity, magnetic and kinetic energies, ohmic and viscous dissipations. Both cases have less variable dipole moments than the Earth. For PADM2M $\sigma_{g_1^0}/\langle g_1^0 \rangle = 28\%$, case 2.2 has $\sigma_{g_1^0}/\langle g_1^0 \rangle = 10\%$, and case 2.2 has $\sigma_{g_1^0}/\langle g_1^0 \rangle = 9.4\%$.

3.3. Asymmetry between growth and decay of axial dipole energy

The two dynamo cases we selected exhibit different skewness properties which are shown in Figure 2 where the skewness coefficients, $s(f_{co})$ are each compared with those of PADM2M.

The main signature in PADM2M is positive skewness across the intermediate frequency range. Neither of the dynamo simulations exactly reproduces the PADM2M results, but Case 2.2 comes the closest. It has significantly positive $s(f_{co})$, over a portion of the intermediate frequency range 0.017-0.045 kyr^{-1} (Figure 2a). Case 2.3 is interesting because the significant skewness it has is negative, which is opposite in sense to PADM2M (Figure 2b). In Case 2.2 several of the distributions of positive and negative rates of change cannot be distinguished at the 95% significance level under the Kolmogorov-Smirnov test as indicated by the open symbols in Figure 2, but the distributions with significant asymmetry in the frequency range 0.017-0.045 kyr^{-1} mostly pass the Kolmogorov-Smirnov test.

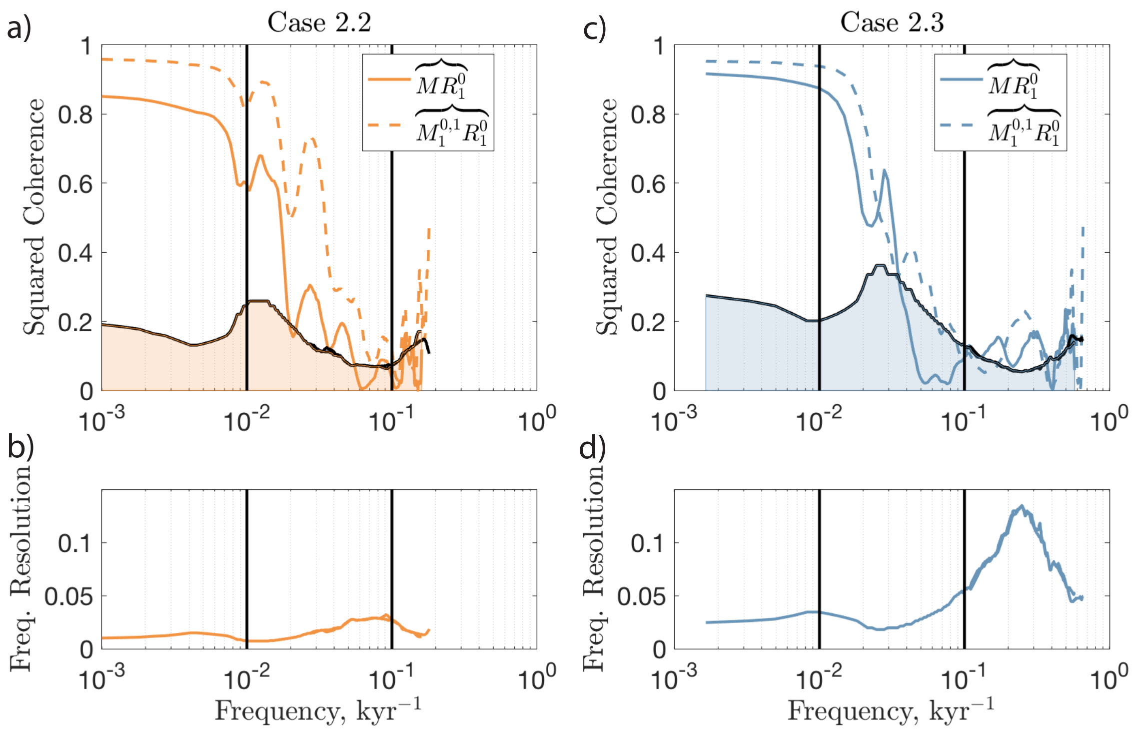

Figure 3: Connection between the total outer-core magnetic energy and surface observable axial dipole energy, i.e. the squared coherence spectra between the magnetic energy (M) and surface dipole energy (R_1^0) for a) Case 2.2 (orange) and c) Case 2.3 (blue). The black line bounding the shaded region indicates the coherence value below which no coherence can be inferred at the 95% confidence level for white noise processes. b) and d) The frequency resolution $\Delta f = \frac{k f_N}{N_f}$ for $\overbrace{MR_1^0}(f)$ where $k =$ the number of tapers, $f_N =$ the Nyquist frequency, and $N_f =$ the number of frequencies estimated.

3.4. Coherence between total magnetic energy and surface axial dipole energy

The toroidal part of the geomagnetic field is unobservable outside of the outer core, so Earth's dipole at the surface will not relay the entirety of the magnetic energy variations. To evaluate this in our dynamo simulations we evaluate the coherence between the total magnetic energy and surface axial dipole energy.

The solid colored lines in Figure 3a–b present the squared coherence as a function of frequency between M, the total magnetic energy in the core, and R_1^0, the energy in the surface axial dipole. The black line and shaded regions of Figure 3a–b show the 95% confidence level for the squared coherence spectra between two white noise processes below which the coherence is considered insignificant. Coherence in the low and intermediate part of the frequency ranges are significant. The frequency resolution for the coherence spectra are plotted in Figure 3c–d were computed by $\Delta f = k f_n / N_f$ where k is the number of tapers used at each frequency, f_n is the Nyquist frequency, and N_f is the number of frequency estimates. Note that for Case 2.3 Δf is well above 0.02 throughout the frequency range, hence we should not give too much credence to the detailed coherence variations below frequencies of $f = 0.02$ kyr^{-1}, for Case 2.2 Δf is between 0.007-0.03 kyr^{-1}.

With the above caveat in mind, at frequencies below 0.01 kyr^{-1} we see consistently high coherence levels between the total magnetic energy in the outer core and the paleomagnetically observable energy in the axial dipole moment. From 0.01 kyr^{-1}, where coherence has already decreased to 0.6 for Case 2.2 and 0.9 for Case 2.3, it drops further below the 95% significance level at 0.055 kyr^{-1} for Case 2.2 and 0.035 kyr^{-1} for Case 2.3, and is essentially negligible at higher frequency. It is not immediately obvious why Case 2.2 (which has lower Ra) exhibits lower overall coherence in all frequency bands than Case 2.3, but there is a clear suggestion that a larger fraction of the energy is concentrated in the axial dipole variations in Case 2.3, possibly due to more vigorous convection (Case 2.3 has a stronger $\langle g_1^0 \rangle$).

In a similar analysis conducted on the core's magnetic energy restricted to the $l = 1$ dipole term and the surface axial-dipole energy ($\overbrace{M_1^{0,1} R_1^0}(f)$) we found overall higher coherence than with the total magnetic energy at long periods as would be expected from exclusion of non-dipole variations in the core (Figure 3a–b dashed lines). In both cases the decay in coherence with increasing frequency is more gradual than the for $\overbrace{MR_1^0}(f)$, with significant coherence for frequencies less than $\sim$0.1 kyr^{-1}.

In both simulations we find that the surface axial-dipole energy is coherent with the total magnetic energy in the core ranging from the longest period assessable to about 30 kyr. When only the dipole components of the core energy are considered the range extends to periods of about 10 kyr.

3.5. Balancing Magnetic Induction against Diffusion

A more detailed frequency domain analysis of the dynamo output based on Equation 2 allows us to examine the various contributions to changes in magnetic energy as a function of frequency. Figure 4a shows the PSD for each term in Equation 2, the rate of change of magnetic energy, $\dot{M}$, the magnetic diffusion, O, and the work done by the Lorentz force L, while Figure 4b provides the associated squared coherence spectra between each of the terms: $\overbrace{OL}(f)$, $\overbrace{\dot{M}O}(f)$, and $\overbrace{\dot{M}L}(f)$.

The general pattern in PSD for both cases is as follows: at low frequency

$\widetilde{O}(f)$ (dashed line) and $\widetilde{L}(f)$ (dotted line) are essentially equal while $\widetilde{\dot{M}}(f)$ (solid line, Figure 4a) plays a relatively unimportant role. The low power seen in $\widetilde{\dot{M}}(f)$ at low frequencies is expected because the Fourier transform of a time derivative of $x(t)$ is the product of $(2\pi i f)$ and the Fourier transform of $x(t)$, $\mathfrak{F}\left[\dot{x}(t)\right] = 2\pi i f \mathfrak{F}\left[x(t)\right]$. The $\widetilde{\dot{M}}(f)$ At intermediate frequency $\widetilde{\dot{M}}(f)$ gains power although $\widetilde{O}(f)$ and $\widetilde{L}(f)$ remain strong, and at high frequency all the terms drop by several orders of magnitude. This rapid fall-off occurs at a higher frequency for Case 2.3 with a higher Ra.

$\overbrace{OL}(f)$ shows high coherence (solid lines in Figure 4b) with O and L out of phase across all frequencies in both simulations. Coherence with $\dot{M}$ grows with increasing frequency over the low frequency range (dashed and dotted lines), but we should keep in mind the average frequency resolution shown in Figure 3b, which suggests the possibility of spectral leakage from the intermediate range. In both cases at high frequency $\dot{M}$ is more coherent with L than O. In the same intermediate frequency range where s is positive for Case 2.2 (0.017-0.045 kyr^{-1}) $\dot{M}$ is more coherent with O than L [$s(f_{co}) > 0$ and $\overbrace{\dot{M}O}(f) > \overbrace{\dot{M}L}(f)$](orange solid rectangle in Figure 4b). In slightly higher frequency ranges than where s is negative for Case 2.3 the derivative of the magnetic energy is more coherent with L than O [$s(f_{co}) < 0$ and $\overbrace{\dot{M}O}(f) < \overbrace{\dot{M}L}(f)$] (blue checkered rectangles in Figure 4b).

At low frequencies Figure 4 supports the idea that not much energy is passed to the magnetic energy, the coherence spectra $\overbrace{\dot{M}L}(f)$ and $\overbrace{\dot{M}O}(f)$ are both low. High frequency magnetic energy changes reflect the work done by the Lorentz force, at high frequency $\dot{M}$ is more coherent with L than O. In the intermediate frequency band we can associate asymmetry properties with changes in coherence behavior: higher coherence between $\dot{M}$ and O occurs where $s > 0$, and higher coherence between $\dot{M}$ and L with $s < 0$.

Variations in ohmic dissipation could be due to variations in the amplitude of the magnetic field (stronger fields lead to higher dissipation) or in the length scale of the magnetic field (magnetic field with small length-scale is readily dissipated). By evaluating the coherence between the ohmic dissipation and the length scales of the magnetic field (ℓ_B) and the non-dimensional amplitudes of the magnetic field (Lo), we find changes in O are more representative of changes Lo than of changes in ℓ_B, though the two factors are linked ($\widehat{OLo}(f) > \widehat{O\ell_B}(f)$, Figure 6a–c).

To summarize, variations in the surface dipole energy (R_1^0), which we can compare with paleomagnetic observations, convey variations in the dipole energy of the outer core ($M_1^{0,1}$) for frequencies less than 0.1 kyr^{-1} and conveys variations in the total magnetic energy for frequencies less than 0.03 kyr^{-1}. In the low and intermediate frequency ranges we should be able to make interpretations about the energy conditions within the outer core from observations recorded at Earth's surface. The asymmetry in $\dot{R}_1^0$ observed in these simulations is linked to the balance between O and L. We also link the variations in the ohmic dissipation with variations in the amplitude of the magnetic field rather than the field's length scale. This indicates that the asymmetry in $\dot{R}_1^0$ is due to variations in the amplitude of the magnetic field rather than a transfer of energy between large and small length scales

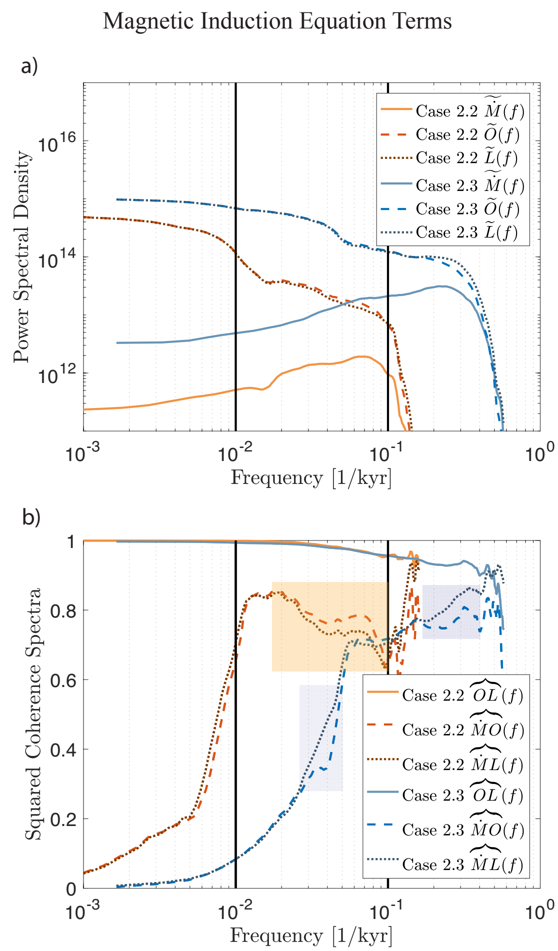

Figure 4: The interplay between terms in the magnetic induction equation. a) The power spectra $\widetilde{\dot{M}}(f)$, $\widetilde{O}(f)$, and $\widetilde{L}(f)$ for Cases 2.2 (orange) and 2.3 (blue). b) The squared coherence spectra between $\dot{M}$, O, and L for Cases 2.2 (orange) and 2.3 (blue). The orange rectangle in b) highlight where Cases 2.2 has $\overbrace{\dot{M}O}(f) > \overbrace{\dot{M}L}(f)$ and positive $s(f_{co})$. The blue checkered rectangles highlight were Cases 2.3 has $\overbrace{\dot{M}O}(f) < \overbrace{\dot{M}L}(f)$, which is similar to the frequency where it has negative $s(f_{co})$ in Figure 2b but shifted $\sim$0.04 kyr^{-1} higher.

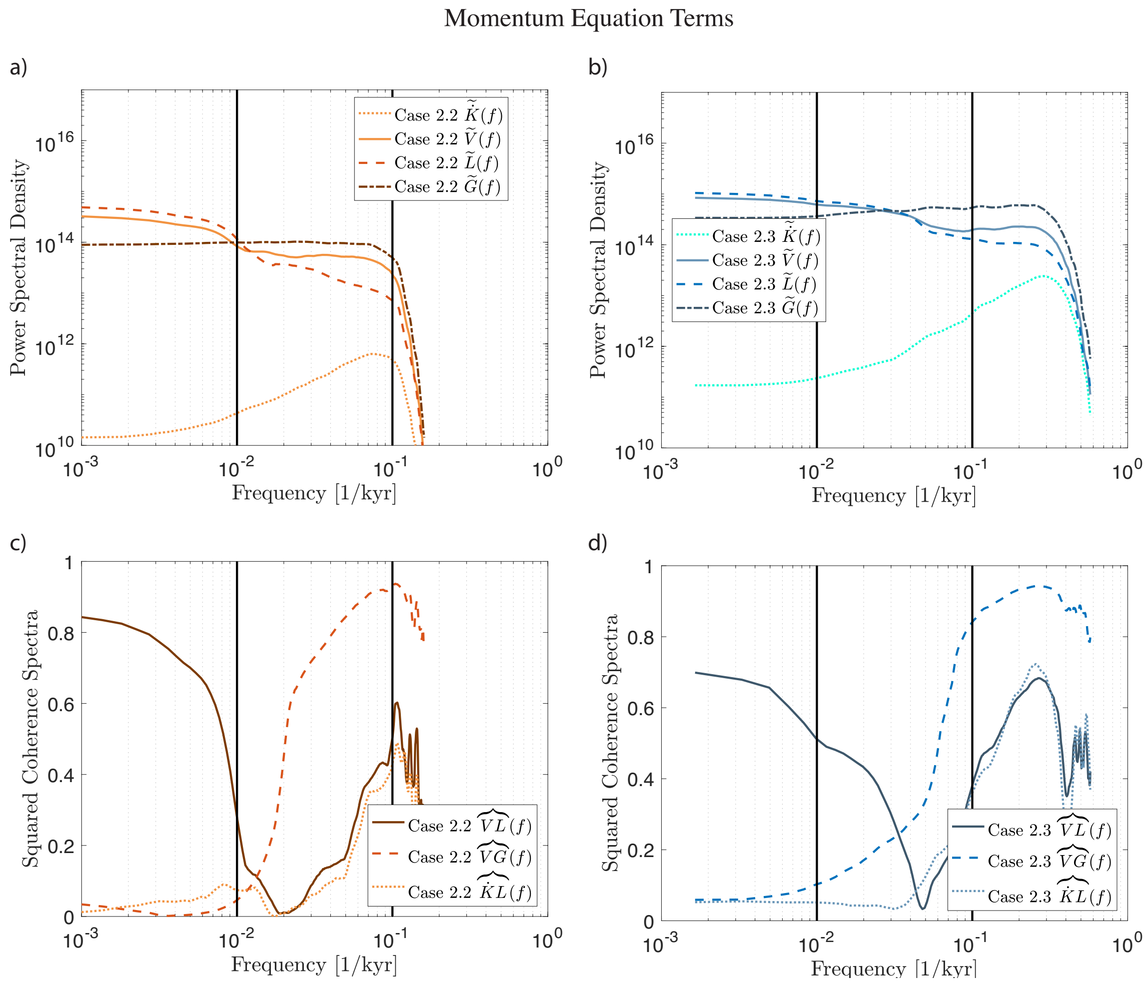

Figure 5: (a–b) The power spectra $\widetilde{\dot K}(f)$, $\widetilde V(f)$, $\widetilde L(f)$, and $\widetilde G(f)$ for a) Cases 2.2 (orange) and b) 2.3 (blue). (c–d) The squared coherence spectra $\overbrace{VL}(f)$, $\overbrace{VG}(f)$, and $\overbrace{\dot KL}(f)$ for c) Case 2.2 (orange), d) Case 2.3 (blue).

3.6. Balance of Momentum Equation

Spectral techniques can also be used to evaluate the balance between terms in the momentum equation (Equation 3). G is the energy source while V and O are energy sinks, and L transfers energy between K and M through dynamo action. Building on our hypothesis of the dynamo being close to a steady state at low frequencies, if $\dot{K}$ and $\dot{M}$ are much smaller than the diffusion and work terms Equation 2 becomes $L \approx -O$, and Equation 3 is then $G \approx O + V$. For the Earth it can be assumed V is negligibly small, but it is not in geodynamo simulations. At intermediate and high frequencies where $\dot{K}$ and $\dot{M}$ grow in power our technique can help us track the path of energy from G to V and O through L, K, and M.

The general pattern in PSD for both cases is as follows (Figures 5a–b): the viscous dissipation $\widetilde{V}(f)$ and the work done by the Lorentz force $\widetilde{L}(f)$ have high power at low frequencies, the buoyancy force $\widetilde{G}(f)$ is lower but significant, and hence changes in the kinetic energy $\widetilde{\dot{K}}(f)$ have low power. At intermediate frequency a transition occurs, power in $\widetilde{\dot{K}}(f)$ grows larger while $\widetilde{V}(f)$ and $\widetilde{L}(f)$ decrease. The frequency where $\widetilde{G}(f)$ overtakes $\widetilde{V}(f)$ and $\widetilde{L}(f)$ in power is lower for Case 2.2. Increasing Ra increases the power in all the terms and shifts variations in the general pattern of the PSDs to higher frequency. This shift of features to higher frequency with higher Ra is also seen in the coherence between the various terms (Figures 5c–d). For both cases at high frequency all the terms drop in power by several orders of magnitude.

For completeness the squared coherence spectra for all combinations of terms of the momentum equation are shown in Supplemental Figure S5. Here we focus on the squared coherence spectra $\widehat{VL}(f)$, $\widehat{VG}(f)$, and $\widehat{\dot{K}L}(f)$ which tell us about the balance of momentum and dynamo operation (Figure 5c–d). For both cases at low frequency $\widehat{VL}(f)$ is high, while $\widehat{VG}(f)$ and $\widehat{\dot{K}L}(f)$ are low. Again based on the frequency resolution, some of the low frequency signal may have leaked from the intermediate range. In the intermediate range $\widehat{VL}(f)$ falls while $\widehat{VG}(f)$ grows. This shift shows the transition from the low frequency quasi-steady state to intermediate frequency dynamo operation. In the high frequency range the PSDs for all terms drop off (Figures 5a–b) and so the results there are not meaningful.

As with changes in O, we test if the variations in viscous dissipation are due to variations in the length scale of the velocity or its amplitude. We expect for example the low frequency variations in V will be associated with variations in large scale zonal winds; they may vary in velocity but have a length scale set by the geometry of core. By comparing $\widehat{VRm}(f)$ and $\widehat{V\ell_u}(f)$ where Rm is the measure of the amplitude of the velocity field and ℓ_u is the length scale of viscous dissipation, we find low frequency changes in V are indeed more representative of changes in amplitude of the velocity field than of changes in dissipation length scale ($\widehat{VRm}(f) > \widehat{V\ell_u}(f)$ Figure 6b and d).

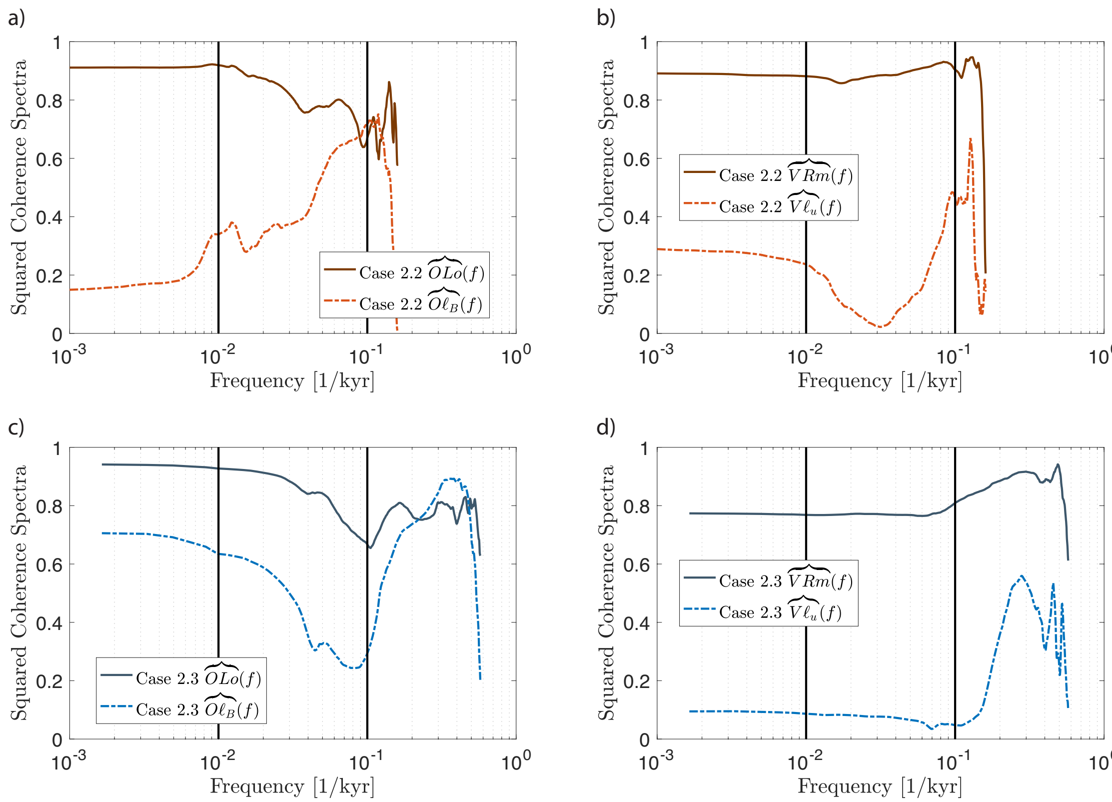

Figure 6: Origin of variations in dissipation, length scale or field amplitude for Case 2.2 (orange) and Case 2.3 (blue). a) and c) $\overbrace{OLo}(f)$ and $\overbrace{O\ell_B}(f)$ where Lo is the measure of the amplitude of the magnetic field and ℓ_B is the length scale of ohmic dissipation. b) and d) $\overbrace{VRm}(f)$ and $\overbrace{V\ell_u}(f)$ where Rm is the measure of the amplitude of the velocity field and ℓ_u is the length scale of viscous dissipation.

4. Discussion

We have developed four tools for evaluating the energy balance of geodynamo simulations: 1) the distribution of time derivatives of the surface axial dipole energy (R_1^0) and summary skewness statistic ($s(f_{co})$), 2) the coherence spectra ($\overbrace{MR_1^0}(f)$) between total magnetic energy of the outer core (M) and the surface axial dipole energy ($\dot{R}_1^0$), 3) the power and squared coherence spectra (indicated with $\tilde{\ }(f)$ and $\overbrace{\ \ \ }(f)$ over-bars respectively) which we apply to both the terms in the magnetic induction equation and the terms in the momentum equation, and 4) the squared coherence spectra between the dissipation terms and the length scale and amplitude of their associated fields.

The buoyancy force and the sum of the dissipation terms have high coherence at all frequencies. The small deviations from this balance are what sustain variations in the magnetic field, which is consistent with the findings of Buffett and Bloxham (2002). The input parameters for our geodynamo simulations produce slightly different energy balances. Cases 2.2 and 2.3 have a buoyancy profile which gives them a moderate cooling rate (69 K/Gyr), and Case 2.3 has a higher Ra than Case 2.2. They both have columnar convection with strong zonal flow, and lack convection inside their tangent cylinders (Davies and Gubbins, 2011).

Davies and Gubbins (2011) determined these dynamos to be Earth-like by comparing them with the paleomagnetic field on the basis of field morphology and their axial dipole moment power spectra, but because of computational limitations they are far from the Earth in non-dimensional parameter space. We use the tools listed above to study them further. This is a pilot study and more work is needed before robust conclusions and inferences to Earth can be drawn. Nevertheless, the present results suggest for time scales longer than $\sim$30 kyr the surface axial dipole energy conveys variations of the total magnetic energy, an important piece of the core's internal dynamics. In our simulations we have identified a connection between $s(f_{co})$ (Figure 2) and the coherence spectra $\widehat{\dot{M}O}(f)$ and $\widehat{\dot{M}L}(f)$ (Figure 4). A higher coherence between $\dot{M}$ and O than between $\dot{M}$ and L corresponds to $s(f_{co}) > 0$, while higher coherence between $\dot{M}$ and L corresponds to $s(f_{co}) < 0$. This correlation shows the effects of induction and diffusion have different frequency signatures on variations of the magnetic field, which are observable at Earth's surface in the axial dipole. The structure of the asymmetry changes with Ra. The observation of asymmetry in Earth's dipole moment between growth and decay is a powerful constraint for geodynamo simulations to reproduce.

$\widetilde{G}(f)$ is nearly constant with frequency across the low and intermediate frequency ranges (Figure 5a–b). G expresses correlations between u_r and temperature, i.e. upwellings and downwellings, so the G results indicate the state of mixing. $\widetilde{G}(f)$ indicates the simulations are well-mixed in the low and intermediate frequency ranges. $\widetilde{V}(f)$ and $\widetilde{L}(f)$ decrease as frequency increases while $\widetilde{\dot{K}}(f)$ increases in power in the intermediate frequency range. This transition out of steady state conditions is also seen by an increase in the coherence spectra $\widehat{VG}(f)$ in the intermediate frequency range. In the low frequency range when $\widetilde{V}(f)$ and $\widetilde{L}(f)$ have high power, the coherence spectra $\widehat{VG}(f)$ is low. The low frequency variations in $\widetilde{V}(f)$ and $\widetilde{L}(f)$ are not due to variations in G. At high frequency L is more coherent with $\dot{M}$, this shows the timescales the frozen-flux approximation may be appropriate for (<10kyr).

At low frequencies the large scale flow structures that develop are predominantly azimuthal (thermal winds, zonal flows) that do not affect u_r or therefore G. If the long time scales are dominated by zonal flow, it would strongly suggest that $\widetilde{V}(f)$ decreasing with frequency reflects changes in flow velocity amplitude (Rm), rather than length scale (ℓ_u) which is set by the size of the outer core. To test this we compute the coherence spectra $\overbrace{VRm}(f)$ and $\overbrace{V\ell_u}(f)$. V is more coherent with Rm than ℓ_u (Figure 6).

Since $Pm \sim 1$, the same argument holds for the magnetic field. Changes in O are more representative of changes in the magnetic field amplitude (Lo) than of changes in magnetic dissipation length scale (ℓ_B) (Figure 6). This indicates that the asymmetry between growth and decay rates of the ADM observed at the surface is due to changes in magnetic field strength and not an exchange between length scales. For the ohmic dissipation the effects of field amplitude and length scale are not as isolated as for the viscous dissipation. The coherence spectra $\overbrace{O\ell_B}(f)$ is higher at low frequencies than the corresponding $\overbrace{V\ell_u}(f)$. Rapid growth R_1^0 may reflect generation of poloidal field by coherent radial motions, while slow decay could reflect diffusion of the large-scale flow that has a long time constant.

5. Conclusions

On periods longer than $\sim$30 kyr the surface dipole energy does convey variations of the total magnetic energy of the dynamo in these simulations, suggesting with long enough observational paleomagnetic models we can also learn about the core's internal dynamics. Some progress can be made by constructing higher order spherical harmonic paleomagnetic models for Myr time spans, but this cannot provide access to toroidal field variations or other important features of the internal dynamics. There is a limit to what we can interpret solely on the basis of observations of the dipole energy made at Earth's surface. This is where the numerical simulations can provide valuable insight.

We have demonstrated that assessing the power spectra and coherences between the various energy contributions in the magnetic induction and momentum equations can be linked to useful insight into the physics underlying some geodynamo simulations. Differences in power between ohmic heating and the work done by the Lorentz force are linked to the frequency dependence of asymmetry between rates of growth and decay of surface axial dipole energy. We have identified test cases with symmetry properties that are similar to and distinct from the paleomagnetic signature in dipole moment variations over the past 2 Myr.

The intermediate frequency range reveals a transition from low frequency steady state to the dynamo operation in the intermediate and high frequency ranges. Viscous and ohmic dissipations decrease in power while the changes in kinetic and magnetic energies increase in power, with increasing frequency. Low frequency power in viscous and ohmic dissipations are shown to originate in variations in the velocity and magnetic field amplitudes rather than field length scales.

We present tools for comparing geodynamo simulations with long-term (Myr) models of paleomagnetic axial dipole variations. The spectral analysis shows case 2.2 is Earth-like in the sense of displaying substantial dipole variations with asymmetry like the Earth's. Case 2.3 has the opposite asymmetry.

Our current study is not exhaustive enough to identify explicitly the dynamical causes of asymmetry in rates of change in Earth's dipole moment, but it does demonstrate a useful analysis method. Studying the energy balance of the geodynamo as a function of frequency is a useful tool. When just high frequency variations and time averages of terms of the energy balance are compared, behavior at intermediate frequencies may be missed. These tools will next be applied to many more geodynamo simulations with a broad range of input parameters, followed by detailed analysis of internal dynamical processes associated with specific symmetry properties.

Acknowledgements

The authors thank Bob Parker for access to his spectral analysis codes. This work was funded by the NSF grant numbers EAR 1065597 and 1623786. CJD is supported by a Natural Environment Research Council Independent Research Fellowship (NE/L011328/1). This work used the Extreme Science and Engineering Discovery Environment (XSEDE), which is supported by National Science Foundation grant number ACI-1053575. We thank Victor Eijkhout and Amit Chourasia for their assistance with optimization and

visualization, which was made possible through the XSEDE Extended Collaborative Support Service (ECSS) program.

References

Avery, M. S., Gee, J. S., Constable, C. G., 2017. Asymmetry in growth and decay of the geomagnetic dipole revealed in seafloor magnetization. Earth and Planetary Science Letters 467, 79–88.
doi: 10.1016/j.epsl.2017.03.020

Bloxham, J., Gubbins, D., 1985. The secular variation of Earth's magnetic field. Nature 317 (6040), 777.
doi: 10.1038/317777a0

Bloxham, J., Jackson, A., 1991. Fluid flow near the surface of Earth's outer core. Reviews of Geophysics 29 (1), 97–120.
doi: 10.1029/90RG02470

Buffett, B., Bloxham, J., 2002. Energetics of numerical geodynamo models. Geophysical Journal International 149 (1), 211–224.
doi: 10.1046/j.1365-246X.2002.01644.x

Cande, S. C., Kent, D. V., 1992. A new geomagnetic polarity time scale for the Late Cretaceous and Cenozoic. Journal of Geophysical Research: Solid Earth 97 (B10), 13917–13951.
doi: 10.1029/92JB01202

Cande, S. C., Kent, D. V., 1995. Revised calibration of the geomagnetic polarity timescale for the Late Cretaceous and Cenozoic. Journal of Geo-

physical Research: Solid Earth 100 (B4), 6093–6095.
doi: 10.1029/94JB03098

Christensen, U. R., Aubert, J., Hulot, G., 2010. Conditions for Earth-like geodynamo models. Earth and Planetary Science Letters 296 (3), 487–496.
doi: 10.1016/j.epsl.2010.06.009

Constable, C., Johnson, C., 2005. A paleomagnetic power spectrum. Physics of the Earth and Planetary Interiors 153 (1), 61–73.
doi: 10.1016/j.pepi.2005.03.015

Constable, C., Korte, M., Panovska, S., 2016. Persistent high paleosecular variation activity in Southern hemisphere for at least 10,000 years. Earth and Planetary Science Letters 453 (7043), 78–86.
doi: 10.1016/j.epsl.2016.08.015

Davies, C., Gubbins, D., 2011. A buoyancy profile for the Earth's core. Geophysical Journal International 187 (2), 549–563.
doi: 10.1111/j.1365-246X.2011.05144.x

Davies, C. J., Constable, C. G., 2014. Insights from geodynamo simulations into long-term geomagnetic field behaviour. Earth and Planetary Science Letters 404, 238–249.
doi: 10.1016/j.epsl.2014.11.045

Finlay, C. C., Aubert, J., Gillet, N., 2016. Gyre-driven decay of the Earth's magnetic dipole. Nature Communications 7.
doi: 10.1038/ncomms10422

Gubbins, D., Alfe, D., Masters, G., Price, G. D., Gillan, M., 2004. Gross thermodynamics of two-component core convection. Geophysical Journal International 157 (3), 1407–1414.
doi: 10.1111/j.1365-246X.2004.02219.x

Johnson, C. L., Constable, C. G., 1998. Persistently anomalous Pacific geomagnetic fields. Geophysical research letters 25 (7), 1011–1014.
doi: 10.1029/98GL50666

Korte, M., Holme, R., 2010. On the persistence of geomagnetic flux lobes in global Holocene field models. Physics of the Earth and Planetary Interiors 182 (3), 179–186.
doi: 10.1016/j.pepi.2010.08.006

Livermore, P. W., Hollerbach, R., Finlay, C. C., 2017. An accelerating high-latitude jet in Earth's core. Nature Geoscience 10 (1), 62–68.
doi: 10.1038/ngeo2859

Lowes, F., 1974. Spatial power spectrum of the main geomagnetic field, and extrapolation to the core. Geophysical Journal International 36 (3), 717–730.
doi: 10.1111/j.1365-246X.1974.tb00622.x

Mound, J., Davies, C., Silva, L., 2015. Inner core translation and the hemispheric balance of the geomagnetic field. Earth and Planetary Science Letters 424, 148–157.
doi: 10.1016/j.epsl.2015.05.028

Nimmo, F., 2015. Energetics of the Core. Treatise on Geophysics 8 (Chapter 2), 27–55.
doi: 10.1016/B978-0-444-53802-4.00139-1

Olson, P., Christensen, U., Glatzmaier, G. A., 1999. Numerical modeling of the geodynamo: mechanisms of field generation and equilibration. Journal of Geophysical Research: Solid Earth 104 (B5), 10383–10404.
doi: 10.1029/1999JB900013

Olson, P. L., Christensen, U. R., Driscoll, P. E., 2012. From superchrons to secular variation: A broadband dynamo frequency spectrum for the geomagnetic dipole. Earth and Planetary Science Letters 319, 75–82.
doi: 10.1016/j.epsl.2011.12.008

Oruba, L., Dormy, E., 2014. Predictive scaling laws for spherical rotating dynamos. Geophysical Journal International 198 (2), 828–847.
doi: 10.1093/gji/ggu159

Parks, T., McClellan, J., 1972. Chebyshev approximation for nonrecursive digital filters with linear phase. IEEE Transactions on Circuit Theory 19 (2), 189–194.
doi: 10.1109/TCT.1972.1083419

Pozzo, M., Davies, C., Gubbins, D., Alfè, D., 2012. Thermal and electrical conductivity of iron at Earth's core conditions. Nature 485 (7398), 355–358.
doi: 10.1038/nature11031

Pozzo, M., Davies, C., Gubbins, D., Alfè, D., 2013. Transport properties for liquid silicon-oxygen-iron mixtures at Earth's core conditions. Physical Review B 87 (1), 014110.
doi: 10.1103/PhysRevB.87.014110

Riedel, K. S., Sidorenko, A., 1995. Minimum bias multiple taper spectral estimation. IEEE Transactions on Signal Processing 43 (1), 188–195.
doi: 10.1109/78.365298

Valet, J.-P., Meynadier, L., Guyodo, Y., 2005. Geomagnetic dipole strength and reversal rate over the past two million years. Nature 435 (7043), 802–805.
doi: 10.1038/nature03674

Willis, A. P., Sreenivasan, B., Gubbins, D., 2007. Thermal core-mantle interaction: Exploring regimes for 'locked' dynamo action. Physics of the Earth and Planetary Interiors 165 (1), 83–92.
doi: 10.1016/j.pepi.2007.08.002

Ziegler, L., Constable, C., 2011. Asymmetry in growth and decay of the geomagnetic dipole. Earth and Planetary Science Letters 312 (3), 300–304.
doi: 10.1016/j.epsl.2011.10.019

Ziegler, L., Constable, C., Johnson, C., Tauxe, L., 2011. PADM2M: a penalized maximum likelihood model of the 0–2 Ma palaeomagnetic axial dipole moment. Geophysical Journal International 184 (3), 1069–1089.
doi: 10.1111/j.1365-246X.2010.04905.x